PNAS
www.pnas.org

Supplementary Information for

Atmosphere-ocean oxygen and productivity dynamics during early animal radiations

Tais W. Dahl,[1*] James N. Connelly,[1,2] Da Li,[3] Artem Kouchinsky,[4] Benjamin C. Gill,[5] Susannah Porter[6], Adam C. Maloof,[7] Martin Bizzarro[1,2]

Corresponding author:
Tais W. Dahl, tais.dahl@snm.ku.dk

This PDF file includes:

Other supplementary materials for this manuscript include the following:

Supplementary Materials

S1. Sample descriptions and geological settings

The Terreneuvian series (Fortunian Stage and Cambrian Stage 2) spans a long time interval, ~539-521 Ma after the Ediacaran and before the Cambrian Stage 3, when trilobites and other arthropods diversified. In Siberia and Mongolia, the time interval is subdivided into the Nemakit-Daldynian and Tommotian intervals, and in South China it is called the Meishucunian. Although, stage boundaries have not yet been globally defined, carbonate isotope stratigraphy show a steady increasing $\delta^{13}C$ trend and two >+5‰ positive excursions in the Pre-Tommotian strata across Siberia, Mongolia and Morocco. The composite $\delta^{13}C$ curve from South China may well be incomplete, since only one isotope excursion greater than +5‰ has been reported (denoted, 'ZHUCE')(1). Maloof et al. 2010 (2) proposed an age model based on ash beds from Morocco, China and Oman, which was subsequently refined with data from Mongolia (3) (Fig S1) and that we use with minor adjustments to fit with sections from China, as described below and in Fig S6.

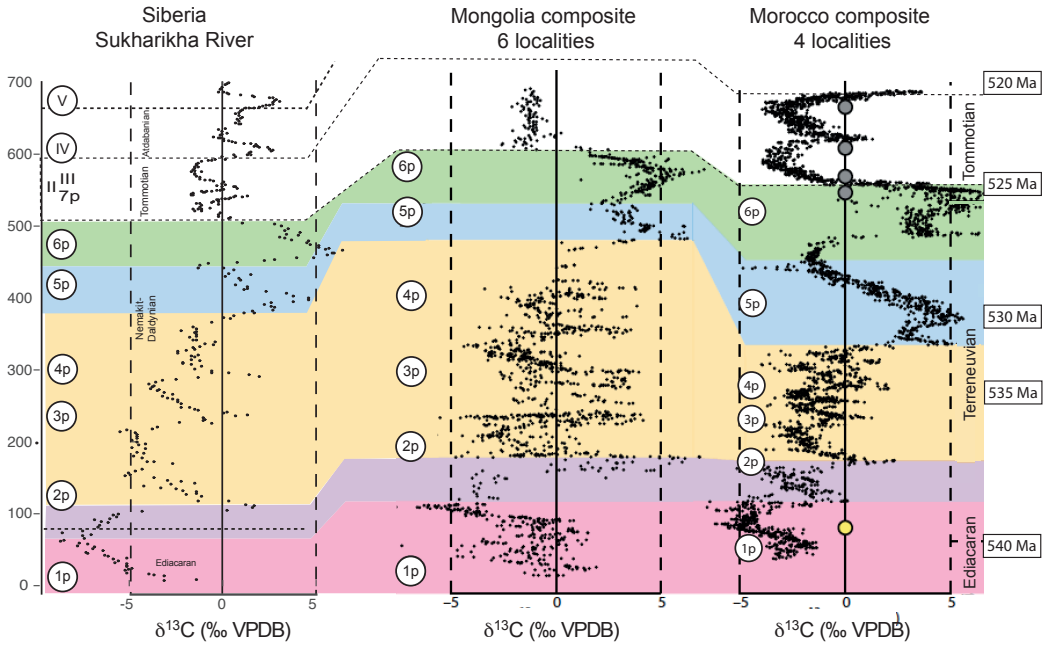

Figure S1. Terreneuvian age model (modified after ref. (2, 4) as described below).

Siberia

The Nemakit-Daldynian to Tommotian interval occurs within the Sukharikha and Krasnoporog formations at the northwestern margin of the Siberian platform (*e.g.,* Sukharikha river), within the Nemakit-Daldyn and Medvezhya formations at the Western Anabar Uplift (*e.g.,* Kotuikan river), within the Manykay and Emyaksin formation of the Eastern Anabar Uplift (*e.g.,*Bol'shaya Kuonamka river), and within the Ust'-Yudoma Formation and Petrotsvet formations in Southeastern Siberian platform (*e.g.,* Lena, Aldan and Selinde river)(5-7).

The studied carbonate samples were collected from three localities across the Siberian platform including 1) Sukharikha River section, Igarka region, northwestern margin of the Siberian Platform, by Vladimir Pavlov and Vladimir Vodovozov from the

Institute of Physics of the Earth, Moscow (67°12.472'N; 87°22.753'E) (8), 2) Ary-Mas-Yuryakh section by AK (70° 08.5′ N, 114° 00′ E, left bank of Kotuj River upstream from mouth of Ary-Mas-Yuryakh Creek) (9, 10), and 3) Bol'shaya Kuonamka river section by AK and S. Bengtson (70°42.4' N, 112°47.2' E) (6). All three sections have been interpreted as open-shelf marine facies (5).

Sukharikha River

The Sukharika river section contains the most complete Siberian record (Fig. S2), and matches the Nemakit-Daldynian to Atdabanian $\delta^{13}C_{CaCO3}$ curve of Morocco and Mongolia peak for peak (Fig. S1) (11). The section comprises of the Sukharikha formation, Krasnaporog formation and the Shumny formations representing an upwards-deepening succession. The Sukharikha formation is interpreted to represent a carbonate proximal ramp deposit based on its dolostones with subordinate limestones, recurring flat pebble conglomerates, domal stromatolites and desiccation-cracked dolo-laminates. The Krasnoporog Formation represents carbonate shelf deposits with bioturbated lime mudstones, local bioherms and biostromes. The Shumny formation consists of mostly dark colored carbonate turbidites and nodular limestones, representative of carbonate slope deposits.

Apart from a mixed dolomitic–terrigenous composition in the uppermost part of the underlying Izluchina Formation and lowermost Sukharikha Formation, the majority of samples consist of predominantly calcite with low Mg/Ca and Mn/Sr indicative of limited marine diagenetic fluid flow through the rocks. Only two out of 51 analyzed samples had slightly elevated Mn/Sr >1 (1.2-1.4). Nineteen samples contained dolomite. The impact of diagenesis on $\delta^{238}U$ is explored further below.

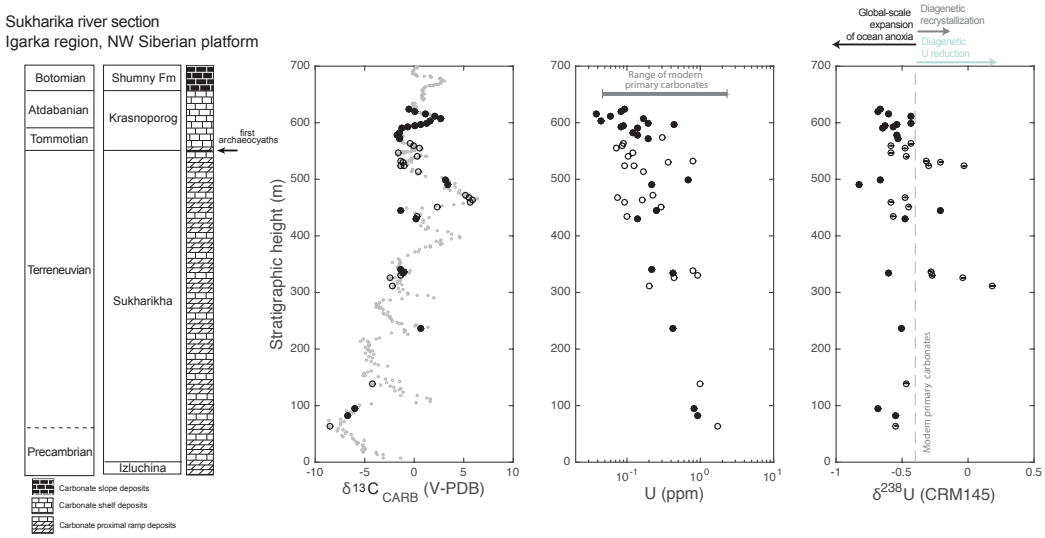

Fig. S2. Isotope data in stratigraphic context for the Sukharika river section, NW Siberia. Samples analyzed for U isotopes are shown in circles with the least altered carbonates shown with black fill. Stratigraphy information from ref. (11).

Kotuikan River

The Kotuikan river section (Fig. S3) record a large positive $\delta^{13}C$ excursion (assigned to I') and two biostratigraphically important fossils that have been proposed to define the base of Cambrian Stage 2, micromollusk (rostroconch) *Watsonella crosbyi* and the

mollusk *Aldanella attleborensis (9, 10)*. Both fossils occur in the Medvezhya formation at the rising limb towards a +5‰ peak. Further, the $\delta^{13}C$ values stay above 0‰ after the excursion. For these reasons, the I' excursion is correlated to the first of the two large Terreneuvian excursions denoted "5p" elsewhere in the world.

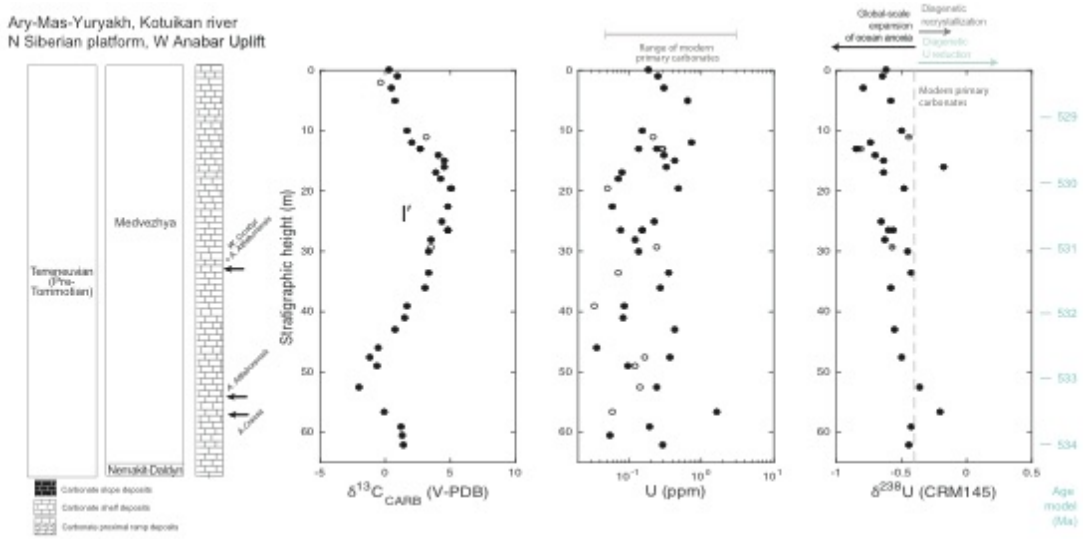

Fig. S3. Isotope data in stratigraphic context for the Kotuikan river section, W Anabar Uplift, N Siberia. Stratigraphy information from ref. (10).

Bol'shaya Kuonamka River

The Kuonamka river section (Datafile S1) represents part of the Emyaksin formation of the eastern Anabar Uplift (Siberia) that can be correlated across the platform by $\delta^{13}C$ chemostratigraphy (6) (where this section is denoted "section 96–5"). The studied samples were collected along the Bol'shaya Kuonamka River covering a large positive $\delta^{13}C$ excursion also assigned to *I′* (6). Due to extremely low U contents, most samples were not analyzed for $\delta^{238}U$.

Stratigraphic correlations in Siberia

The Siberian sections have been correlated to one another using chemo- and biostratigraphy (6, 11, 12). The first occurrence of *A. Attleborensis* and *W. Crosbyi* occurs in sections from the Anabar uplift at the rising limb of a large positive carbon isotope excursion. Although the Cambrian Stage 1–2 boundary is still not formally defined, it is these features that have been proposed to define the base of the Cambrian Stage 2 (9).

The absence of biostratigraphic fossils at Sukharikha River and the incompleteness of the other (chemo)-stratigraphic records compromises reliable correlation between I' at the Anabar Uplift and other large positive carbon isotope excursions, such as 5p or 6p at Sukharikha River (and elsewhere in the world). However, the 5p excursion likely correlates with a +5‰ positive $\delta^{13}C$ excursion in the *N. Sunnaginus* zone of the uppermost Mattaia Formation at the Olenyok uplift on the Eastern Siberian platform. Here, a U-Pb zircon age of 529.7±0.3 Ma is reported at the peak of the $\delta^{13}C$ excursion that sits below another large >4‰ positive $\delta^{13}C$ excursion (13-15). The overlying 6p excursion is constrained in Morocco, where ash beds with U-Pb ages of 525.34 ± 0.09 and 524.84 ± 0.09 Ma occur at the 6‰ peak and at the 0‰-crossing of the falling limb, respectively.

South China

Two sections ~200 km apart from the Meishucunian Stage of South China were studied at Xiaotan (Fig. S4) and Laolin (Fig. S5), Yunnan, SW China. The Xiaotan section covers late Ediacaran to Cambrian Stage 3 strata. Here, we studied only the limestone of the Dahai Member in the Zhujiaqing Formation. The Dahai Member comprises pale, thickly-bedded limestone and contains *Heraultipegma yunnanensis* [=Watsonella crosbyi (Grabau, 1900)] Assemblage (Zone III) small shelly fossils (SSFs). The first occurrence datum of *Heraultipegma yunnanensis* (base of Cambrian Stage 2?) has been located at the rising limb (near the 0‰ crossing) of large positive $\delta^{13}C$ excursions reaching maxima of +7‰ (P4) and +4‰ (L4) in the Xiaotan and Laolin sections, respectively. These two isotope excursions are considered coeval (P4 = L4) and can be referred to by the name 'ZHUCE': the last large $\delta^{13}C$ peak in the Zhujiaqing Formation before a drop to negative $\delta^{13}C$ values (1, 16). The ZHUCE is thought to be late pre-Tommotian in age as it shares some common fossils with the Siberian *N. sunnaginicus* zone (17). These sections were not previously included in Terreneuvian age models (2, 4). At present, a correlation between ZHUCE and 6p elsewhere in the world is sensible, but this needs to be confirmed. New U-Pb data from ash beds within the Xiaotan section from the rising and falling limbs of the 'ZHUCE' excursion show ages of 527.0 ±? Ma and 526.1±? Ma, respectively (18).

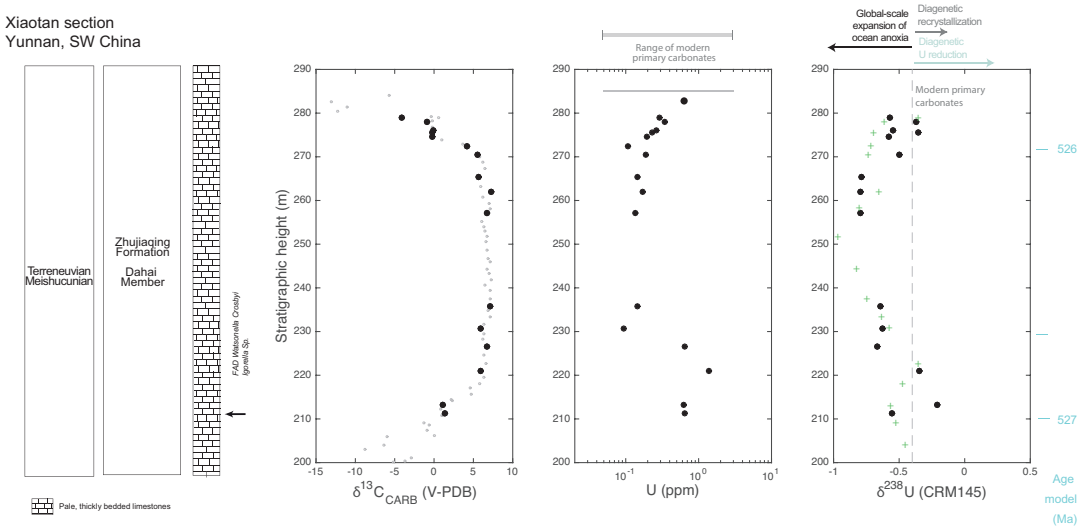

Fig. S4. Isotope data in stratigraphic context for the Xiaotan section, Yunnan, SW China. Stratigraphic information from ref. (19). Uranium isotope data collected at Yale (+) is correlated to data obtained in Copenhagen, but with a slope distinct from unity. An inter-laboratory round-robbin of shared carbonate reference materials is now needed to resolve this issue.

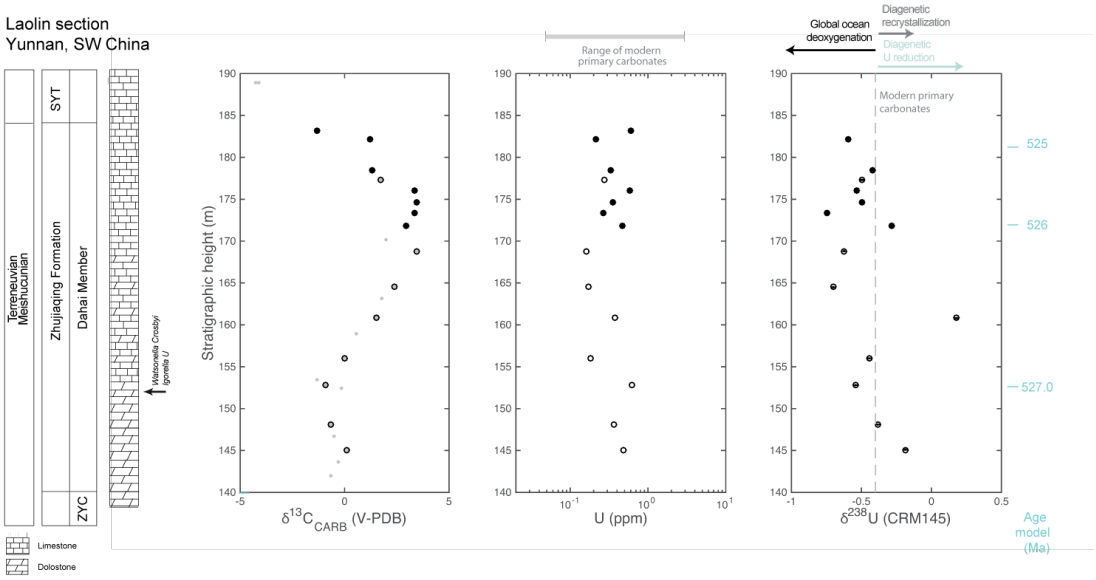

Fig. S5. Isotope data in stratigraphic context for the Laolin section, Yunnan, SW China. Stratigraphic information from ref. (19).

Stratigraphic correlations in China. The Xiaotan and Laolin sections both record the 'ZHUCE' carbon isotope excursion. Our age model ensures that changes in $\delta^{13}C$ curves are correlated, but differences in sedimentation rate can produce offsets in the age model when $\delta^{13}C$ does not change. For example, there is ~50 m in Xiaotan section with constantly high $\delta^{13}C$, whereas Laolin has no long plateau. Therefore, we adjusted the sedimentation rate to ensure that both $\delta^{13}C$ and $\delta^{238}U$ trends are optimally correlated (Fig. S6).

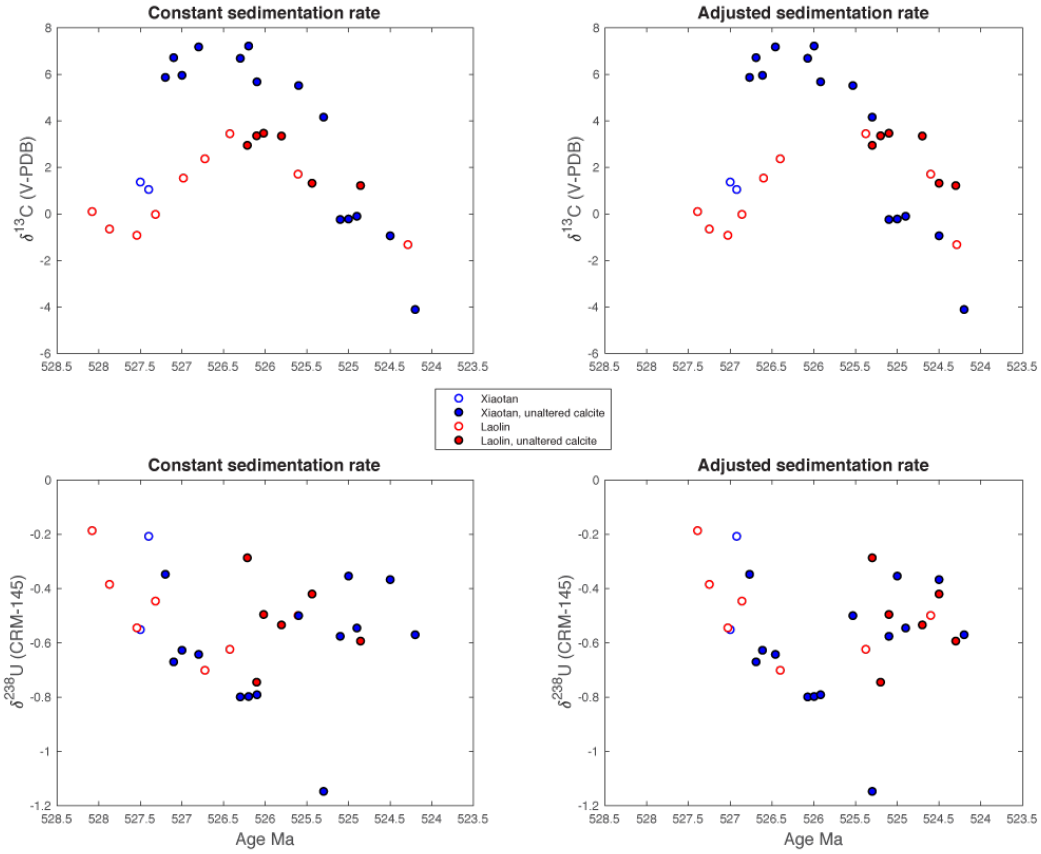

Fig. S6. Stratigraphic correlation between Laolin and Xiaotan sections

Morocco

The Terreneuvian interval occurs within the Adoudounian and Lie de Vin formations of the Taroudant Group in the western Anti-Atlas margin of Morocco. Our samples come from the Oued Sdas section (Fig. S7).

The Tifnout Member of the Adoudounian formation consist of predominantly peritidal dolostones arranged in metre-scale, shallowing upwards parasequences that typically begin with siltstones and marls followed by wavy laminated micrites and grainstones, and are capped with microbialaminites and stromatolites commonly showing signs of subaerial exposure (2, 20). The Tifnout Member is barren of diagnostic fossils for biostratigraphical correlations, but it contains two ash beds with accurate U-Pb zircon ages.

The Lie de Vin formation represents a significant sea-level regression with sublittoral deposition of purple argillite, and stromatolitic or thrombolitic limestone bioherms with calcified algae, such as *Tarthinia*, *Renalcis*, and *Kordephyton (21, 22)*. A 10 cm thick tuff at a stratigraphic height of 1031 m in Oued Sdas has a weighted mean $^{206}Pb/^{238}U$ age of 523.17±0.16 Ma (MSWD = 1.2). A 5-cm-thick tuff within a 2.2-m-thick thrombolite bioherm at a stratigraphic height of 1536 m in the upper Lie de Vin Formation has a weighted mean $^{206}Pb/^{238}U$ age of 520.93±0.14 Ma (2)
The oldest known skeletal fossils from Morocco, including trilobites of the *Eofallotaspis* zone, occur at ~1900 m in the stratigraphy in the overlying Igoudine Formation (20).

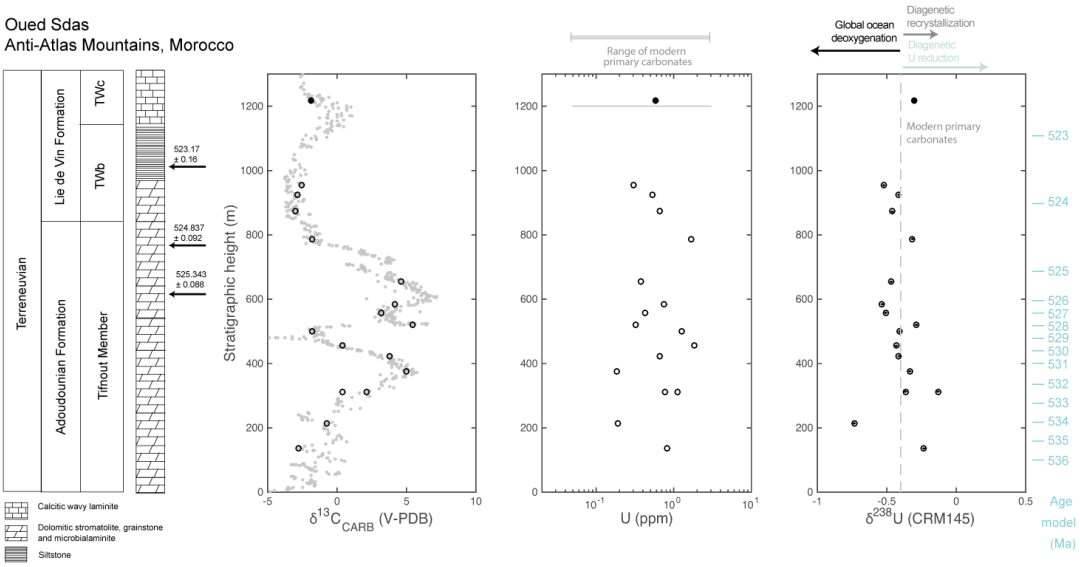

Fig. S7. Isotope data in stratigraphic context for the Oued Sdas section, Anti-Atlas Mtns, Morocco. Stratigraphic information from ref (20).

S2. Diagenetic processes affecting $^{238}U/^{235}U$ in carbonates.

Primary carbonate minerals incorporate trace amounts of uranium with the same isotope composition as the seawater in which they grew (23, 24). A small isotope fractionation, up to +0.13‰, occur in co-precipitation experiments with aragonite at pH 8.5. No resolvable U isotope fractionation is observed in co-precipitation experiments with aragonite at pH 7.5 or with calcite at either pH (25). Aragonite and high-magnesium calcite are metastable phases on >1 Myr time scales and are subsequently converted into low-Mg calcite and/or dolomite (26, 27). This conversion is one of the most critical early diagenetic transitions especially given that the partition coefficients for U into low Mg calcite and dolomite is much lower than for aragonite and high-Mg calcite, resulting in preferential loss of U from the recrystallized sediments.

In the Bahamas carbonates, bulk carbonate sediments within the uppermost 10 cm carries a +0.27±0.14‰ offset from $\delta^{238}U$ in overlying seawater (23, 28). This offset results from a partial U loss and either U(VI) reduction in the sulphate reducing zone or preferential removal of U(VI) carbonate anions during carbonate dissolution and recrystallization under distinct pore water chemistry (e.g. Ca^{2+}, Mg^{2+}, CO_3^{2-}). In both cases, these processes occur during early (syndepositional) diagenesis on the banktop, when solutes exchange in an open system manner between pore fluids and overlying seawater. Later stage diagenesis appears to have smaller influence on U isotope variability, presumably because reductive immobilization to U(IV) phases stabilizes U in the carbonate matrix. Meteoric diagenesis also appears to have negligible effect on carbonate $\delta^{238}U$ due to the low U concentration in terrestrial fluids (28). In the Bahamas, there is no correlation between the $\delta^{238}U$ offset from contemporaneous seawater and various diagenetic proxies(28). We explore this further below.

S2.1 Model prediction for carbonate diagenesis and statistical tests

A simple model of carbonate diagenesis in the presence of seawater suggest that the order in which concentrations and isotope compositions are altered as a function of fluid rock ratio is: $\delta^{18}O$ (fluid/rock > 1), $^{87}Sr/^{86}Sr$ and Mn/Sr (fluid/rock >10–100),

$\delta^{238}U$ (fluid/rock >100–1000) and $\delta^{13}C$ (fluid/rock ~ 1000–10,000) (29). Therefore, Mn/Sr is a diagnostic indicator for samples that have experienced extensive diagenetic fluid replacement that potentially also influenced the U isotope composition. Due to the contrasting sensitivities to the fluid/rock ratio, this type of diagenetic fluid replacement is not expected to produce correlations between these geochemical parameters, but high Mn/Sr is still diagnostic of altered samples distinguishable from (tentatively) unaltered samples. Below, we explore the hypothesis that diagenetic U dissolution and reprecipitation from seawater-derived fluids will lead to higher $\delta^{238}U_{CAU}$ values in the samples (whether by U(VI) reduction or U(VI) recrystallisation).

First, we confirm the bimodal distribution of Mn/Sr and Mg/Ca in our sample set (with far the majority of samples being unaltered limestone with low Mn/Sr). Contrary, the $\delta^{18}O$ distribution is unimodal with a wide variance around the mean. Secondly, we compare average $\delta^{238}U_{CAU}$ values for unaltered and altered samples to confirm that $\delta^{238}U_{CAU}$ is significantly higher in the altered pool of samples. We find that samples with Mn/Sr > 1 has an average $\delta^{238}U_{CAU}$ value of –0.39±0.26‰ (1sd, n= 27) compared to –0.53±0.20‰ (1 sd, n=77) for samples with lower Mn/Sr. A Welch's t-test confirm that the altered and unaltered samples have distinct mean values at p = 0.0043. Similarly, dolomitic samples with Mg/Ca > 0.1 display a higher average $\delta^{238}U_{CAU}$ of -0.40± 0.20‰ (1 sd, n = 44) than calcitic samples with lower Mg/Ca at $\delta^{238}U_{CAU}$ –0.54±0.20‰. (1 sd, n = 81). Again, the mean values are statistically distinct at the p = 0.0007. Therefore, these proxies qualify as useful predictors for diagenetic alteration associated with a positive $\delta^{238}U_{CAU}$ offset from contemporaneous seawater, and we can use these to filter out (at least some) samples.

S2.2 A note on U isotope fractionation during dolomitization. The formation of dolomite from calcitic and aragonitic precursor minerals requires interaction with marine fluids that could potentially disturb $\delta^{238}U_{CAU}$. An example from the Fortunian (Cambrian Stage 1) part of the Sukharika river section may reflect such a process. Here, dolomite beds bracket a limestone bed, suggesting either dolomitisation or de-dolomitisation occurred at an early diagenetic stage. Clearly, the dolomitic sediments are associated with a systematic +0.3‰ $\delta^{238}U$ offset that may reflect either U reduction or recrystallization (28).

Similarly, we observe a dolomitized sample with distinctly higher $\delta^{238}U$ than adjacent samples (A258, $\delta^{238}U$ = -0.03±0.05‰), and higher than the maximum value for seawater (that is ~ –0.3‰, given oceanic U input with $\delta^{238}U$ similar to today and an oceanic U inventory at near steady-state). We conclude that the high $\delta^{238}U$ value was produced locally during early diagenesis. Nevertheless, this sample has a low Mn/Sr ratio of 0.4 indistinguishable from unaltered samples, showing that the Mn/Sr diagenetic proxy alone is unable to identify all diagenetically altered samples.

The combination of Mn/Sr and Mg/Ca proxies may seem appealing. However, it should be stressed that dolomitized samples do not always display a $\delta^{238}U$ offset relative to adjacent limestones. For example, one partly dolomitized limestone with an elevated Mn/Sr ratio (A294, $\delta^{238}U$ = –0.46±0.03‰, Mn/Sr = 2.5) falls exactly on the $\delta^{238}U$ trend in limestones with low Mn/Sr across the Nemadit Daldynian – Tommotian boundary. Therefore, we cannot consider all dolomites as useless as paleooceanic $\delta^{238}U$ recorders. Further, Late Permian dolomites from Dawen, China

(30) also preserve essentially identical $\delta^{238}U$ trends to that observed in limestones elsewhere in the world (29-31). At present it is unclear when dolomites record $\delta^{238}U$ value of overlying seawater.

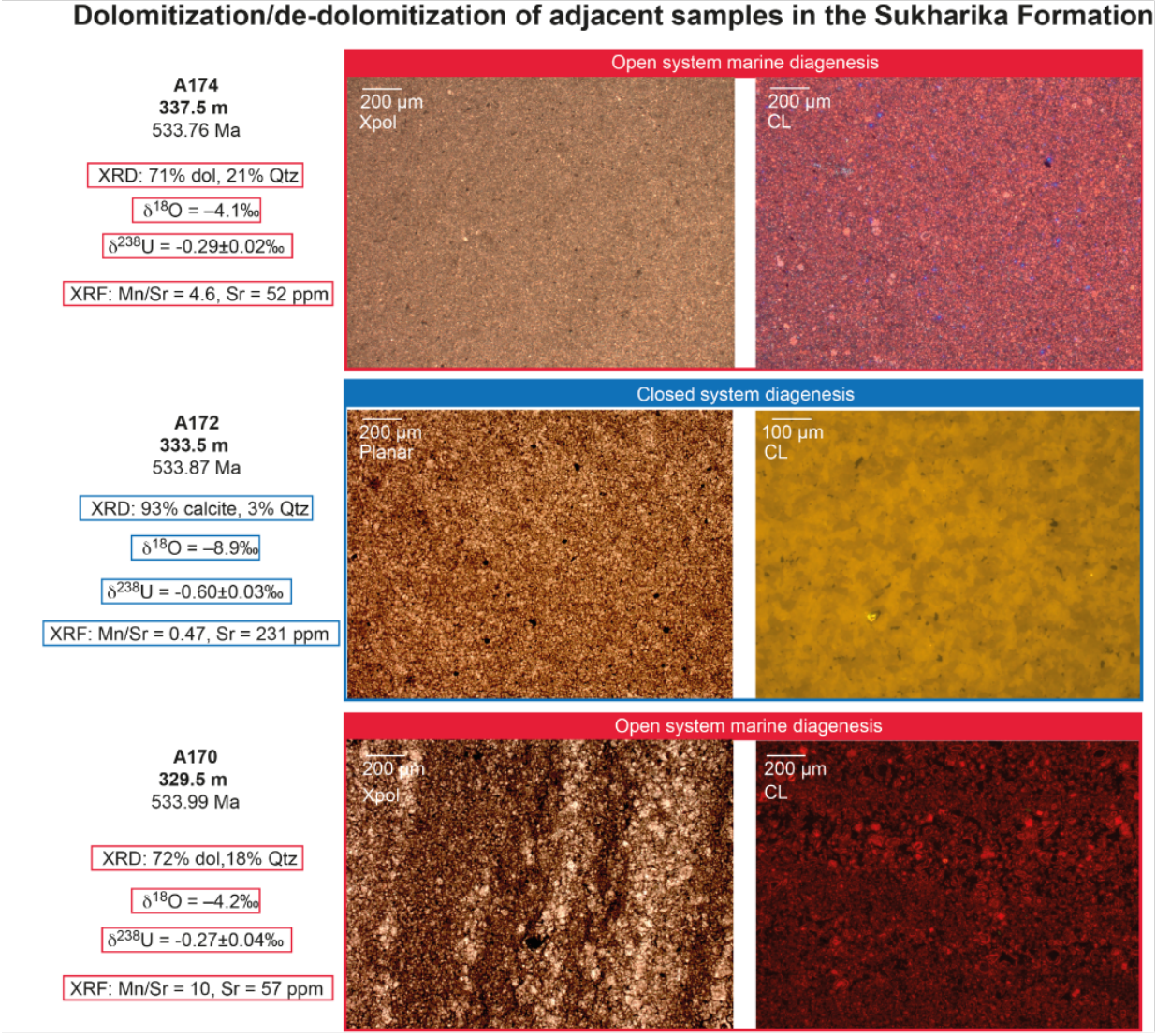

Figure S8. Petrographic analyses of three samples (337.5 to 329.5 m) in the Sukharikha Fm and comparison to $\delta^{238}U_{CAU}$, mineralogical and diagnostic geochemical data (Mn/Sr, $\delta^{18}O_{CARB}$).

S3. $\delta^{238}U$ record of Terreneuvian seawater

The carbonate $\delta^{238}U$ record constrains $\delta^{238}U$ of Terreneuvian seawater, and we explore various ways to correct for the early diagenetic offset. Previous workers have made various assumptions about this effect, including no offset (23, 29), a constant +0.3‰ offset (32), or a variable and sulphate-dependent offset (33) between sediments and overlying seawater. Our best chance is to collect large, high-resolution data sets in sediment $\delta^{238}U$ values to average out stochastic variations in individual bulk sediment samples.

First, we fit a spline curve through $\delta^{238}U$ of the least altered limestone samples (Fig. 2). The spline curve is smooth and oscillates in concert with the global marine $\delta^{13}C$ record. This $\delta^{238}U_{LAC}$ curve. Still, early diagenetic processses might offset the sediments to higher values than in contemporaneous seawater. For example, three samples (T1-16, T1-56.5, A221) carry distinctly higher $\delta^{238}U$ values than adjacent samples, the spline curve, and the expected range for seawater (< –0.3‰), supporting our previous conclusion that no diagnostic measures perfectly distinguish samples with a $\delta^{238}U$ offset from contemporaneous seawater.

Secondly, we fit a smooth curve, $\delta^{238}U_{MIN}$, through the minimum values of all data within 0.4 My intervals (Fig 2). Importantly, this $\delta^{238}U_{MIN}$ curve parallels the $\delta^{238}U_{LAC}$ curve and reproduces the negative $\delta^{238}U$ excursions. The offset between the $\delta^{238}U_{LAC}$ and $\delta^{238}U_{MIN}$ curves, up to ~0.25‰, is only 0.09‰ smaller than the observed offset between Bahamas banktop carbonates and modern seawater (Figure S9). Therefore, we conclude that the $\delta^{238}U_{MIN}$ curve resemble Terreneuvian seawater with only a small average offset of 0.09‰.

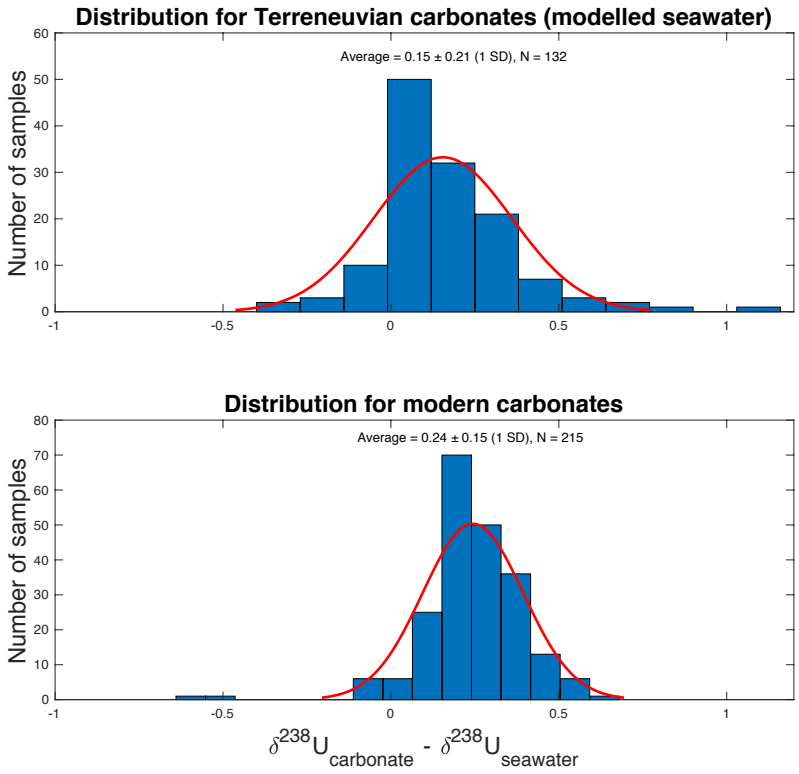

Figure S9. Marine carbonate sediments display a positive $\delta^{238}U$ offset relative to overlying seawater. The distribution of this offset in A) the Terreneuvian data set, assuming d238U$_{MIN}$ resembles Terreneuvian seawater is similar to that of B) modern carbonates from Bahamas cores 1-4 (23), Clino, Unda (28) and ODP drill core 1006A (34). A small, but significant, difference of 0.09‰ exists between the average offset in the two data sets (two-sample t-test, $p = 10^{-6}$) can be explained by a selective bias in the Terreneuvian sample set that favor samples that experienced less post-depositional chemical alteration and slightly smaller offset. Conclusively, the scatter in our data set is natural and $\delta^{238}U_{MIN}$ is a realistic representation of Terreneuvian seawater d238U with a small average offset of 0.09‰.

S4. Local biases on the shale-based paleoredox U proxy

Uranium enrichments in shales display increasing maximum values from 560 to 520 million years (Fig. S11). This was previously used as evidence for steadily increasing O_2 inventory in the oceans (35). However, the amplitude of the U enrichments is far greater than can be ascribed to changes in oceanic inventory and the record is systematically biased due to increasing total organic content (TOC) known to be associated with efficient U capture in the sediments. Once corrected for the TOC bias, the oceanic U inventory appears to have declined across the Ediacaran-Cambrian boundary in agreement with isotope records.

S4.1 Effect of anoxia on the oceanic U pool

Oxygenated oceans are associated with higher U concentrations because the U burial rate in sediments deposited in anoxic basins (109-328 μg cm^{-2} kyr^{-1}) is 15±10 times higher than in oxygenated settings with anoxic pore fluids (9-20 μg cm^{-2} kyr^{-1}) (36). Therefore, an expansion of anoxic sediment burial at the globally integrated scale is expected to draw down the oceanic U pool. The change of the oceanic U inventory depends on the difference in the U accumulation rate between anoxic and oxic settings (~15±10) and how the average U burial rate responds when the uranium concentration in the overlying seawater, [U], declines.

Mathematically, the oceanic inventory (M_U) is determined from the balance between input (J_{IN}) and outputs (J_{OUT}). The burial output flux depends on the size of the inventory, for example we may assume $J_{OUT} = a \cdot M_U^{y}$. Ignoring all other sinks than anoxic settings, the oceanic uranium inventory is given by:

$$dM_U/dt = J_{IN} - a \cdot M_U^{y} \quad \text{(eq. 6)}$$

The steady state inventory ($dM_U/dt = 0$) is:

$$M_{U,\,term} = (F_{IN} / a)^{1/y} \quad \text{(eq. 7)}$$

Here, y is the sensitivity of U accumulation rate in sediments to oceanic inventory. The value of y can be constrained from U burial rates in modern anoxic brackish-water settings with various U concentrations in the overlying waters (Fig. S10).

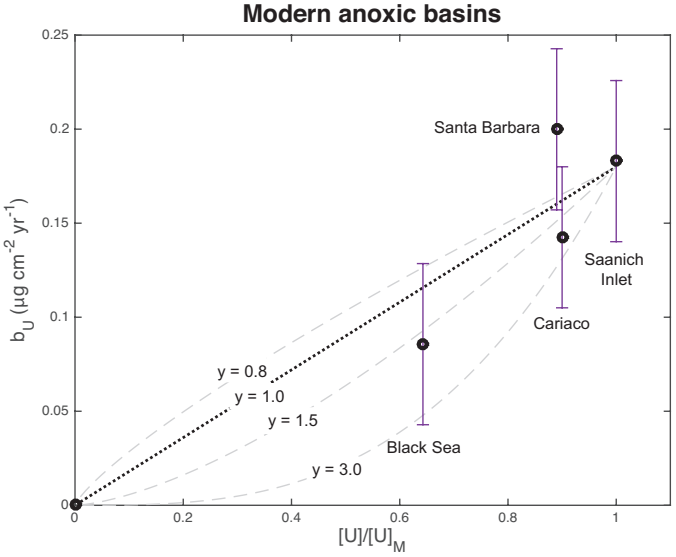

Fig. S10. Uranium burial rate in some modern anoxic basins (b_U) versus the U concentration in overlying waters normalized to open ocean (13 nM). Various

curves $b_U = a \cdot U/U_M^y$ with y ranging from 0.8 to 3 show the burial response to declining U inventory (y) is approximately linear. The U concentration in overlying waters relative to open oceans decrease in the following order: Saanich inlet (1.00), Cariaco Trench (0.90), Santa Barbara basin (0.89), and Black Sea (0.64), and the corresponding U burial rates (μg cm^{-2} yr^{-1}) follows approximately linearly (0.18±0.04, 0.20±0.04, 0.14±0.04 and 0.09±0.04). References: Saanich inlet (37, 38), Cariaco Trench (39), Santa Barbara basin (37) and the Black Sea (40).

Figure S10 shows that the U burial rate in modern open anoxic marine settings correlate with U concentration in overlying waters. Here, more restricted and brackish basins are diluted with respect to U due to the low U concentrations in freshwater. Assuming burial rates are not governed by changes in TOC, we infer that $y \approx 1$ and rule out $y < 0.8$.

At a constant oceanic U input, the maximum reduction of the marine uranium inventory would be $(15\pm10)^{1/y} \approx 30$ (7 –55). This extreme scenario could potentially happen if the entire seafloor changed from oxic to anoxic and the inventory sensitivity was $y = 0.8$. However, the largest Phanerozoic oceanic anoxic events are predicted to cause only a 2–4 fold decrease in the oceanic U pool (29, 33).

S4.2 Observed variability in organic mudrocks

The uranium content in shales varies dramatically from 3 to 1700 ppm (600-fold) during the Ediacaran-Cambrian transition, – and even within a single basin. Clearly, this variation cannot be ascribed to changes in the global extent of anoxia alone. The average U enrichment and U/Th ratio increase with time (across four 20 Myr time bins), but the large variability within each time bin shows that the increase of the mean value is insignificant. Instead, the variability is strongly influenced by local enrichment and preservation processes as evident from U-TOC correlation in the samples (41).

The U-TOC co-variation is also evident in modern environments (42). When corrected for the TOC-bias (e.g. U/TOC), we find that the variability of the mean, max, median and 90-percentile between time bins are all within the range of realistic variability of the oceanic inventory (~3–12 fold). Although, the results are still statistically insignificant, the trend shows that the oceanic U inventory actually declined during the Neoproterozoic–Cambrian transition (Fig. S9). This conclusion is perfectly consistent a long-term atmospheric pO_2 decline until the latest Terreneuvian.

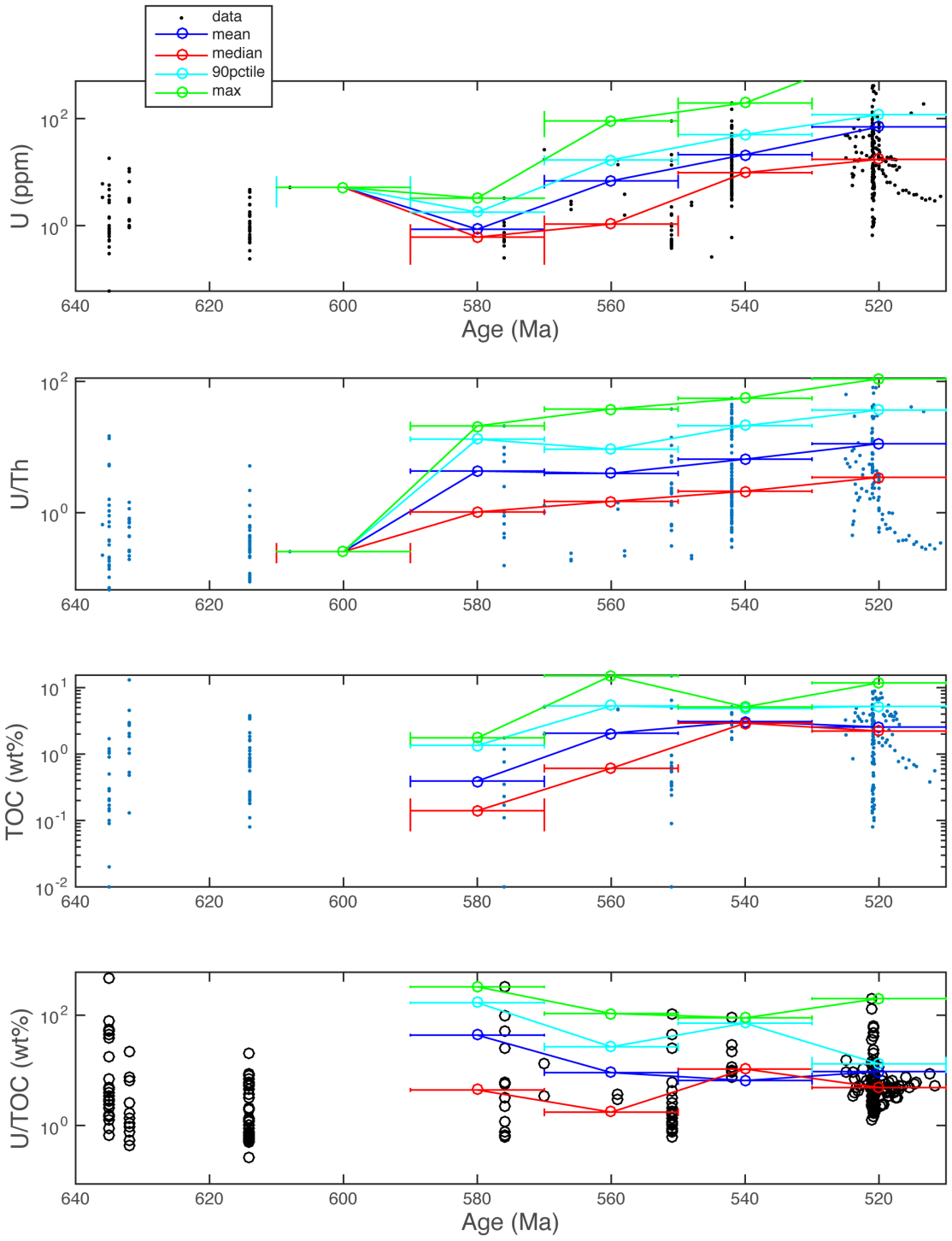

Figure S11: Uranium, U/Th, TOC and U/TOC enrichments in shales (data from ref (41)). Note: although U enrichments in shales increase across the Neoproterozoic-Cambrian transition, so does TOC. Correcting for TOC-bias, suggest that the oceanic U pool did not increase during this time interval.

S5. Simulating seawater δ^{98}Mo from the δ^{238}U record

The marine molybdenum and uranium cycle both respond to increasing anoxic sediment burial at a globally integrated scale. Therefore, the combination of seawater δ^{98}Mo and δ^{238}U curves provide improved constraints on global anoxic sediment burial. In fact, the two proxies provide upper and lower estimates on the extent of anoxia because both increases as a function of oceanic oxygenation state and local overprints are uni-directional and operate in opposite directions on the two isotope systems. The carbonate δ^{238}U record is biased to a more oxygenated ocean state (overestimating seawater δ^{238}U) whereas the δ^{98}Mo record obtained from euxinic mudrocks is biased to a more anoxic ocean state (underestimating seawater δ^{98}Mo). In combination, these records can bracket the global redox evolution of the oceans. Here, we follow up on previous work and describe how seawater δ^{98}Mo and δ^{238}U may be connected (43).

S5.1 The marine U isotope budget

The fraction of total sedimentary U burial occurring in anoxic settings is called f_U and at steady state the oceanic isotope mass balance $\delta_{IN} = \delta_{OUT}$ yields (see derivation in ref. (43)):

$$\delta_{SW,U} = \delta_{IN,U} - f_U \cdot \Delta_{ANOX,U} - (1-f_U) \cdot \Delta_{OTHER,U} \quad \text{(eq. 8)}$$

The isotope composition of each sink, δ_i relates to the isotope composition of contemporaneous seawater (δ_{SW}) via the average isotope offsets (Δ_i) expressed during sediment burial in each sink (note: $\Delta_{i,U}$ is defined as a positive number, so that $\delta_{SW,U}$ decreases with more burial in fractionated (oxic) settings. The magnitude of fractionation increases from oxic ("other", including carbonates) to anoxic environments ($\Delta_{ANOX,U} > \Delta_{OTHER,U}$):

$$\delta_{ANOX,U} = \delta_{SW,U} + \Delta_{ANOX,U} \quad \text{(eq. 9)}$$
$$\delta_{OTHER,U} = \delta_{SW,U} + \Delta_{OTHER,U} \quad \text{(eq. 10)}$$

Here, the isotope composition of oceanic input, $\delta_{IN,U}$, is assumed equal to modern rivers and crustal rocks (–0.30±0.03‰) and the average isotope offsets are assumed constant and equal to today $\Delta_{ANOX,U} = 0.5\pm0.1$‰, $\Delta_{OTHER,U} = 0.01\pm0.06$‰ given f_U = 12-25% and $\delta_{SW,U} = -0.39\pm0.02$‰ today (44, 45). (The stated uncertainties are propagated errors, 2SE, using the equation 6 and the error propagation rule).

S5.2 The marine Mo isotope budget

The fraction of total sedimentary Mo burial occurring in euxinic settings is called f_{Mo}. In steady state three sinks describe the isotope mass balance for the entire oceans: oxic, sulphidic at depth inside the sediments (SAD) and euxinic settings. Sediment burial with Mn-oxides is a major Mo sink, but is of subordinate importance for the marine U budget (45, 46). Molybdenum isotopes are strongly fractionated during Mn-oxide burial (–2.9‰) whereas smaller isotope fractionation (–1‰) occurs in SAD settings. If we define the Mn-oxide fraction of all oxic burial, $\gamma = f_{OX,Mo} / [f_{OX,Mo} + J_{SAD,Mo}]$, then the Mo isotope composition of seawater at steady state is given by:

$$\delta_{SW,Mo} = \delta_{IN,Mo} + f_{Mo} \cdot \Delta_{EUX,Mo} + (1-f_{Mo}) \cdot [\gamma \cdot \Delta_{OX,Mo} + (1-\gamma) \cdot \Delta_{SAD,Mo}] \quad \text{(eq. 11)}$$

Again, the magnitude of isotope fractionation associated with burial in each sink is defined as a positive number ($\Delta_{i,Mo} = \delta_{SW,Mo} - \delta_{i,Mo}$). The magnitude of fractionation increases from anoxic (euxinic) to oxic environments ($\Delta_{OX,Mo} > \Delta_{SAD,Mo} > \Delta_{EUX,Mo}$). Therefore, seawater δ^{98}Mo and δ^{238}U increases as a function of oxygenated seafloor at the globally integrated scale because the lighter Mo and U isotopes are preferentially removed into the sediments in oxygenated settings.

S5.3 Coupling the marine U and Mo isotope budgets

The Mo and U burial fluxes in anoxic settings will be correlated in anoxic environments where hydrogen sulphide is present. Recently, we suggested the correlation between the anoxic burial fractions for U and Mo of total marine sediment burial (f_U, f_{Mo}) is described by a power law that yields 0 and 1 when all sediment burial occurs in oxic and anoxic (euxinic) settings, respectively (43). The exponent a = 1.34±0.38 was obtained by calibration in the modern marine Mo and U budgets.

$$f_{Mo} = f_U^{\,a} \qquad \text{(eq. 12)}$$

A note on sediments with intermediate redox conditions. Molybdenum and U burial fluxes are also coupled in oxic SAD settings, but due to the smaller magnitude of isotope fractionations than in the extreme oxic and anoxic settings, we ignore this in the following derivation.

In anoxic and non-sulphidic settings (ferruginous), we expect a decoupling of U and Mo burial, because reductive U removal occurs already in the Fe reducing zone, whereas Mo removal and capture in sediments requires high sulphide concentrations. Ferruginous conditions existed in parts of the Cambrian oceans (47), but the global extent of these settings is unconstrained. By ignoring the ferruginous sink, we tend to overestimate f_{Mo} using eq. 11, because a fraction of anoxic U burial, f_U, will not be associated with concomitant Mo burial.

S5.4 Comparison of model and data. We calculate seawater δ^{98}Mo curves (eq. 11) and compare with data obtained from sedimentary rocks. The calculated seawater trajectories depend also on the magnitude of fractionation associated with oxic burial. We define $\gamma = f_{OX}/(f_{OX}+f_{SAD})$ the proportion of oxic to total burial in all oxic settings in order to distinguish between oxic burial with Mn-oxides, f_{OX}, associated with large isotope fractionation (–2.9‰) and oxic burial into reducing sediments with smaller fractionation (–0.8‰).

The comparison of data and model (Fig. 4B) suggest that oxic burial with Mn-oxides were higher (= 50-75%) prior to the OAEs and modest (γ = 0-25%) after the events in agreement with declining atmospheric pO_2 levels. These γ estimates are, however, overestimated because anoxic and ferruginous settings are associated with high U burial but not with correspondingly high Mo burial. Therefore, the f_{Mo} estimates applied in equation 8 are too high (associated with smallest isotope fractionation relative other settings), and to compensate for that γ (and f_{OX}) values (associated with the largest isotope fractionation) is overestimated.

Although, the size of the Mn-oxide sink (f_{OX}) is overestimated, it cannot be negligible. This is clear from the maximum δ^{98}Mo values in the sedimentary record which exceeds the oceanic input by 1.5‰ which is twice of that observed in SAD settings (48). Therefore, we conclude that the Mn-oxide Mo burial sink was substantial, especially before the OAEs.

S6. Simulating atmospheric pO_2 levels in the Terreneuvian

The atmospheric O_2 inventory can be modeled from the balance between its sources and sinks. We know that O_2 production through oxygenic photosynthesis in cyanobacteria, algae and plants is kept in almost perfect balance with oxic respiration. A small offset from balance amounts to about 1 part in 1000 where excess organic matter and pyrite sulphur is buried in the crust (49). This burial of organic matter and pyrite in sediments represents the primary long-term sources of atmospheric O_2. Over the course of Earth history, this O_2 source has caused a net oxidation of Earth's oceans and atmosphere. The major O_2 sinks are reducing gasses emanating from Earth's interior and weathering of reducing compounds (including pyrite and organic matter) (50). The O_2 sinks are changing in concert with global fluxes of volcanic outgassing (e.g. seafloor spreading) and submarine and subaerial weathering rates (e.g. continental uplift). These sinks would also affect seawater $^{87}Sr/^{86}Sr$ record. The monotonous $^{87}Sr/^{86}Sr$ record suggest relatively constant atmospheric O_2 sinks in the Fortunian followed by an abrupt shift towards more continental weathering relative to hydrothermal alteration of ocean crust from the Tommotian onwards (Fig. 3).

S6.1 Atmospheric oxygen release from the carbon cycle

The global burial flux of organic carbon can be derived from seawater $\delta^{13}C$ record (in the following abbreviated δ_C) and its derivative (51) as a function of average C isotope offset between seawater and buried organic matter (Δ_C), $\delta^{13}C$ of weathering input (δ_W) and the oceanic C inventory (M_C (51).

$$J_{ORG} = 1/\Delta_C \, [W_C \, (\delta_C - \delta_{W,C}) + d(\delta_C)/dt \, M_C] \qquad \text{(eq. 2)}$$

When the atmospheric O_2 sinks are constant, O_2 release from the carbon cycle is then given by the change J_{ORG} only.

$$dO_2/dt = J_{ORG} - R_{W,ORG} \cdot W_C \qquad \text{(eq. 13)}$$

where $R_{W,ORG}$ is the organic proportion of total carbon weathering (W_C). The change in atmospheric pO_2 is derived integrating the long term O_2 release flux:

$$\Delta O_2 = \int [dO_2/dt \,] dt \qquad \text{(eq. 14)}$$

The result is shown in Figure 5.

S6.2 Atmospheric oxygen release from the sulfur cycle

The global burial flux of reduced sulfur (pyrite) can be calculated from seawater $\delta^{34}S$ record (in the following abbreviated δ_S) and its derivative as a function of average S isotope offset between seawater and sedimentary pyrite (Δ_S), $\delta^{34}S$ of weathering input ($\delta_{W,S}$) and the oceanic S inventory (M_S) (51).

$$J_{PY} = 1/\Delta_S \, [W_S \, (\delta_{W,S} - \delta_S) - d(\delta_S)/dt \, M_S] \qquad \text{(eq. 15)}$$

The O_2 release from the sulphur cycle is then given by

$$dO_2/dt = 15/8 \, (J_{PY} - R_{W,PY} \cdot W_S) \qquad \text{(eq. 16)}$$

so that $\Delta O_2 = \int [dO_2/dt \,] dt$.

The factor 15/8 comes from the stoichiometry between O_2 release and S buried during of pyrite burial:

$$2Fe_2O_3 + 8\, SO_4^{2-} + 16\, H^+ = 15\, O_2 + 4FeS_2 + 8\, H_2O \qquad \text{(eq. 17)}$$

This gives 15 O_2 for every 8 molecules of SO_4^{2-} that gets reduced (52).

The result (Fig. 5) shows how O_2 release from the marine sulphur cycle evolved in the Terreneuvian.

S6.3 Sensitivity analysis

A sensitivity analysis of the model shows that atmospheric pO_2 is particularly sensitive to the total weathering flux and secondly to marine sulfate inventory. Values for the Cambrian have been estimated to ~1/4 and ~1/10 of modern-day values (43, 53, 54), respectively. The organic fraction of total carbon weathered, $R_{W,ORG}$, is critical, since it can leads to atmospheric pO_2 decline. We used the average R_{ORG} value obtained for Cambrian marine organic carbon burial ($R_{W,ORG} = f_{ORG} = 0.2$) and interpret derived negative organic carbon burial fluxes as deviations from average. For the other parameters the adopted uncertainties, including net isotope fractionation associated with sediment burial (Δ_C, Δ_S uncertain by ±5‰) (43), isotopic composition of the inputs ($\delta_{W,C}$ and $\delta_{W,S}$ uncertain by ±1‰ and ± 8‰, respectively)(43), and marine inorganic carbon inventory (MC x 3.8) (2), only affect the estimated atmospheric pO_2 change to a lesser degree (< ±1-2 atm%).

S6.4 Evolution of the marine strontium cycle (and weathering regime)

The marine Sr inventory (M_{Sr}) and $^{87}Sr/^{86}Sr$ (R_{Sr}) reflect the balance between sources and sinks, which we use to constrain relative changes in weathering regime in the Terreneuvian.

$$dM_{Sr}/dt = W_{Sr\text{-}R} + W_{Sr\text{-}DC} + W_{Sr\text{-}HT} - J_{Sr\text{-}BURIAL} \quad \text{(eq. 18)}$$

The major sources of Sr to the oceans are rivers ($W_{Sr\text{-}R}$), ocean crustal hydrothermal activity ($W_{Sr\text{-}HT}$) and marine diagenetic carbonates ($W_{Sr\text{-}DC}$). The marine Sr burial flux is expressed in terms of the marine Sr inventory and the residence time in the ocean (τ_{Sr} > 1 Myr).

$$dM_{Sr}/dt = W_{Sr\text{-}R} + W_{Sr\text{-}DC} + W_{Sr\text{-}HT} - M_{Sr} / \tau_{Sr} \quad \text{(eq. 19)}$$

The residence time is far greater than ocean mixing time scales, thus Sr is well mixed in the oceans and seawater carries a uniform Sr concentration and isotope composition.

The $^{87}Sr/^{86}Sr$ ratio of seawater is determined from the isotope composition of the weathering sources (R_i), diagenetic carbonates (DC) and hydrothermal weathering at the seafloor (HT). The main Sr sink (marine carbonate burial) is assumed to record the isotope composition of overlying seawater:

$$d[R_{Sr} \cdot Sr]/dt = R_{Sr\text{-}R} \cdot W_{Sr\text{-}R} + R_{Sr\text{-}DC} W_{Sr\text{-}DC} + R_{Sr\text{-}HT} \cdot W_{Sr\text{-}HT} - R_{Sr} \cdot M_{Sr} / \tau_{Sr} \quad \text{(eq. 20)}$$

Equation 19 and 29 can be combined to express changes in the oceanic $^{87}Sr/^{86}Sr$ pool:

$$dR_{Sr}/dt = 1/M_{Sr} \; [(R_{Sr\text{-}R} - R_{Sr}) \cdot W_{Sr\text{-}R} + (R_{Sr\text{-}DC} - R_{Sr}) \cdot W_{Sr\text{-}DC} + (R_{Sr\text{-}HT} - R_{Sr}) \cdot W_{Sr\text{-}HT}] \quad \text{(eq. 3)}$$

Our model parameters are first calibrated at modern-day 'aragonitic' ocean (subscript '0' refers to today) to yield the modern Sr inventory with a residence time of 2.4 My at modern day weathering fluxes (Datafile S3). The Terreneuvian ocean state was then modelled by time-variable forcing functions, $q_i(t)$, relative to a aragonitic model ocean state with the same oceanic residence time of strontium as in the modern aragonitic ocean (when $q_{tau} = 1$).

$W_{Sr\text{-}R} = q_R \cdot W_{Sr\text{-}R,0}$ eq. 21
$W_{Sr\text{-}DC} = q_{DC} \cdot W_{Sr\text{-}DC,0}$ eq. 22
$W_{Sr\text{-}HT} = q_{HT} \cdot W_{Sr\text{-}HT,0}$ eq. 23
$\tau_{Sr} = q_{tau} \cdot \tau_{Sr,0}$ eq. 24

We fit the model to $^{87}Sr/^{86}Sr$ constraints on seawater composition by modulating forcing functions (Fig. 2). This shows that a 20% increase in continental weathering alone is sufficient to cause the inflection at ~524 Ma. The magnitude of enhanced

weathering could be even smaller if the isotope composition of material being weathered also changed.

Data file captions

Data files S1. Experimental data from samples analyzed in this study.

Data file S2. Sensitivity analysis of the atmospheric pO_2 model.
Parameter values have been changed one at a time from the modern values (case M) to the best-estimated Cambrian scenarios (C0, C1 marked in green). The net effect on atmospheric pO_2 release from 541–520 Ma and 536-520 Ma are shown (highlighted in blue) together with the amplitude of atmospheric pO_2 change (maximum – minimum). The importance of any of the parameters on atmospheric pO_2 can be seen from comparing two adjacent columns. Lower weathering rate (W1 vs. M) reduce the amplitude of atmospheric pO_2 change linearly with respect to both O_2 release from the C and S cycles. A higher average organic proportion in rocks being weathered (W2 vs. W1) promotes atmospheric pO_2 decline from the C cycle. The smaller marine S inventory in the Cambrian (W2 vs. C0 or C1) reduces the impact of the S cycle on atmospheric pO_2, whereas a greater marine dissolved inorganic carbon (DIC) pool essentially does not change the outcome.

Data file S3. Parameter values used in oceanic mass balance models

Supplementary references

1. Zhu M-Y, Babcock LE, & Peng S-C (2006) Advances in Cambrian stratigraphy and paleontology: Integrating correlation techniques, paleobiology, taphonomy and paleoenvironmental reconstruction. *Palaeoworld* 15(3-4):217-222.
2. Maloof AC*, et al.* (2010) The earliest Cambrian record of animals and ocean geochemical change. *Geological Society of America Bulletin* 122(11-12):1731-1774.
3. Bold U*, et al.* (2016) Neoproterozoic stratigraphy of the Zavkhan terrane of Mongolia: The backbone for Cryogenian and early Ediacaran chemostratigraphic records. *American Journal of Science* 316(1):1-63.
4. Smith EF, Macdonald FA, Petach TA, Bold U, & Schrag DP (2016) Integrated stratigraphic, geochemical, and paleontological late Ediacaran to early Cambrian records from southwestern Mongolia. *Geological Society of America Bulletin* 128(3-4):442-468.
5. Rowland SM*, et al.* (1998) Biostratigraphy of the Vendian–Cambrian Sukharikha River section, northwestern Siberian Platform. *Can. J. Earth Sci.* 35:339–352.
6. Kouchinsky A*, et al.* (2001) Carbon isotope stratigraphy and the problem of a pre-Tommotian Stage in Siberia. *Geological Magazine* 138(04).
7. Varlamov AI*, et al.* (2008) The Cambrian system of the Siberian Platform. (Ministry of OF NATURAL RESOURCES OF THE RUSSIAN FEDERATION, Moscow – Novosibirisk).
8. Kouchinsky A*, et al.* (2007) Carbon isotope stratigraphy of the Precambrian–Cambrian Sukharikha River section, northwestern Siberian platform. *Geol. Mag.* 144(3):1–10.
9. Landing ED & Kouchinsky A (2016) Correlation of the Cambrian Evolutionary Radiation: geochronology, evolutionary stasis of earliest Cambrian (Terreneuvian) small shelly fossil (SSF) taxa, and chronostratigraphic significance. *Geological Magazine* 153(04):750-756.
10. Kouchinsky A*, et al.* (2017) Terreneuvian stratigraphy and faunas from the Anabar Uplift, Siberia. *Acta Palaeontologica Polonica* 62.
11. Kouchinsky A*, et al.* (2007) Carbon isotope stratigraphy of the Precambrian–Cambrian Sukharikha River section, northwestern Siberian platform. *Geological Magazine* 144(04).
12. Kouchinsky A*, et al.* (2005) Pre-Tommotian age of the lower Pestrotsvet Formation in the Selinde section on the Siberian platform: carbon isotopic evidence. *Geological Magazine* 142(04).
13. Cui H*, et al.* (2016) Redox-dependent distribution of early macro-organisms: Evidence from the terminal Ediacaran Khatyspyt Formation in Arctic Siberia. *Palaeogeography, Palaeoclimatology, Palaeoecology* 461:122-139.
14. Marusin V (2016) Ископаемые следы жизнедеятельности из пограничных отложений венда и кембрия Оленекского поднятия Сибирской платформы: Диссертация ... кандидата геолого-минералогических наук. PhD (Novosibirsk, Russia, A.A. Trofimuk Institute of Petroleum Geology and Geophysics SB RAS).
15. Kaufman A*, et al.* (2012) A shorter fuse for the Cambrian explosion? in *GSA Annual Meeting* (Charlotte).

16. Zhu M, Strauss H, & Shields GA (2007) From snowball earth to the Cambrian bioradiation: Calibration of Ediacaran–Cambrian earth history in South China. *Palaeogeography, Palaeoclimatology, Palaeoecology* 254(1-2):1-6.
17. Zhu MY (2001) Early Cambrian stratigraphy of East Yunnan, southwestern China : a synthesis. *Acta Palaeontologica Sinica* 40:4-39.
18. Zhu MY*, et al.* (2017) Insight into the base of the Cambrian: New data from South China and Siberia. *International Symposium on the Ediacaran–Cambrian Transition 2017*, ed McIlroy D, p 137.
19. Li DA*, et al.* (2009) New carbon isotope stratigraphy of the Ediacaran–Cambrian boundary interval from SW China: implications for global correlation. *Geological Magazine* 146(04).
20. Maloof AC, Schrag DP, Crowley JL, & Bowring SA (2005) An expanded record of Early Cambrian carbon cycling from the Anti-Atlas Margin, Morocco. *Canadian Journal of Earth Sciences* 42(12):2195-2216.
21. Latham A & Riding R (1990) Fossil evidence for the location of the Precambrian/Cambrian boundary in Morocco. *Nature* 344:752–754.
22. Bertrand-Sarfati J (1981) Problème de la limite Précambrien-Cambrien: la section de Tiout (Maroc); les stromatolites et leur biostratigraphie (SCHMITT 1979): critiques et observations. *Newsletters on Stratigraphy* 10(1):20-26.
23. Romaniello SJ, Herrmann AD, & Anbar AD (2013) Uranium concentrations and 238U/235U isotope ratios in modern carbonates from the Bahamas: Assessing a novel paleoredox proxy. *Chemical Geology* 362:305-316.
24. Stirling CH, Andersen MB, Potter E-K, & Halliday AN (2007) Low-temperature isotopic fractionation of uranium. *Earth and Planetary Science Letters* 264(1-2):208-225.
25. Chen X, Romaniello SJ, Herrmann AD, Wasylenki LE, & Anbar AD (2016) Uranium isotope fractionation during coprecipitation with aragonite and calcite. *Geochimica et Cosmochimica Acta* 188:189-207.
26. Morse J (2003) Formation and Diagenesis of Carbonate Sediments. *Treatise on geochemistry* 7:67–85.
27. Morse JW & Mackenzie FT (1990) *Geochemistry of Sedimentary Carbonates* (Elsevier Science).
28. Chen X*, et al.* (2018) Diagenetic effects on uranium isotope fractionation in carbonate sediments from the Bahamas. *Geochimica et Cosmochimica Acta* 237:294-311.
29. Lau KV*, et al.* (2016) Marine anoxia and delayed Earth system recovery after the end-Permian extinction. *Proc Natl Acad Sci U S A* 113(9):2360-2365.
30. Brennecka GA, Herrmann AD, Algeo TJ, & Anbar AD (2011) Rapid expansion of oceanic anoxia immediately before the end-Permian mass extinction. *Proc Natl Acad Sci U S A* 108(43):17631-17634.
31. Zhang F*, et al.* (2018) Congruent Permian-Triassic δ238U records at Panthalassic and Tethyan sites: Confirmation of global-oceanic anoxia and validation of the U-isotope paleoredox proxy. *Geology* 46(4):327-330.
32. Elrick M*, et al.* (2017) Global-ocean redox variation during the middle-late Permian through Early Triassic based on uranium isotope and Th/U trends of marine carbonates. *Geology* 45(2):163-166.
33. Dahl TW*, et al.* (2014) Uranium isotopes distinguish two geochemically distinct stages during the later Cambrian SPICE event. *Earth Planet Sci Lett* 401:313-326.

34. Tissot FLH*, et al.* (2018) Controls of eustasy and diagenesis on the 238U/235U of carbonates and evolution of the seawater (234U/238U) during the last 1.4 Myr. *Geochimica et Cosmochimica Acta* 242:233-265.
35. Sperling EA*, et al.* (2013) Oxygen, ecology, and the Cambrian radiation of animals. *Proc Natl Acad Sci U S A* 110(33):13446-13451.
36. Dunk R, Mills R, & Jenkins W (2002) A reevaluation of the oceanic uranium budget for the Holocene. *Chemical Geology* 190:45–67.
37. Zheng Y, Anderson R, van Geen A, & Fleisher M (2002) Remobilization of authigenic uranium in marine sediments by bioturbation. *Geochimica et Cosmochimica Acta* 66(10):1759–1772.
38. Anderson R, Fleisher M, & LeHuray A (1989) Concentration, oxidation state, and particulate flux of uranium in the Black Sea. *Geochimica et Cosmochimica Acta* 53:2215–2224.
39. Andersen MB*, et al.* (2014) A modern framework for the interpretation of 238U/235U in studies of ancient ocean redox. *Earth and Planetary Science Letters* 400:184-194.
40. Romaniello S (2012) Incorporation and Preservation of Molybdenum and Uranium Isotope Variations in Modern Marine Sediments. PhD (Arizona State University, Tempe, AZ).
41. Partin CA*, et al.* (2013) Large-scale fluctuations in Precambrian atmospheric and oceanic oxygen levels from the record of U in shales. *Earth and Planetary Science Letters* 369-370:284-293.
42. McManus J*, et al.* (2006) Molybdenum and uranium geochemistry in continental margin sediments: Paleoproxy potential. *Geochimica et Cosmochimica Acta* 70(18):4643-4662.
43. Dahl TW*, et al.* (2017) Reorganisation of Earth's biogeochemical cycles briefly oxygenated the oceans 520 Myr ago. *Geochemical Perspectives Letters*:210-220.
44. Tissot FLH & Dauphas N (2015) Uranium isotopic compositions of the crust and ocean: Age corrections, U budget and global extent of modern anoxia. *Geochimica et Cosmochimica Acta* 167:113-143.
45. Andersen MB, Stirling CH, & Weyer S (2017) Uranium Isotope Fractionation. *Reviews in Mineralogy and Geochemistry* 82(1):799-850.
46. Kendall B, Dahl TW, & Anbar AD (2017) The Stable Isotope Geochemistry of Molybdenum. *Reviews in Mineralogy and Geochemistry* 82(1):683-732.
47. Zhang Y*, et al.* (2017) Marine redox stratification during the early Cambrian(ca. 529-509 Ma) and its control on the development oforganic-rich shales in Yangtze Platform. *Geochemistry, Geophysics, Geosystems* 18:2354–2369.
48. Dahl TW*, et al.* (2010) Devonian rise in atmospheric oxygen correlated to the radiations of terrestrial plants and large predatory fish. *Proceedings of the National Academy of Sciences of the United States of America* 107(42):17911-17915.
49. Hedges JL & Keil RG (1995) Sedimentary organic matter preservation: an assessment and speculative synthesis. *Mar. Chem.* 49:81–115.
50. Catling DC (2014) The Great Oxidation Event Transition. *Treatise on Geochemistry*), pp 177-195.
51. Kurtz AC, Kump LR, Arthur MA, Zachos JC, & Paytan A (2003) Early Cenozoic decoupling of the global carbon and sulfur cycles. *Paleoceanography* 18(4):n/a-n/a.

52. Berner RA (2006) GEOCARBSULF: A combined model for Phanerozoic atmospheric O2 and CO2. *Geochimica et Cosmochimica Acta* 70(23):5653-5664.
53. Moulton K & Berner R (1998) Quantification of the effect of plants on weathering: Studies in Iceland. *Geology* 25(10):895–898.
54. Quirk J*, et al.* (2015) Constraining the role of early land plants in Palaeozoic weathering and global cooling. *Proc Biol Sci* 282(1813):20151115.